 doi:10.20944/preprints202104.0641.v1

Article

Three-dimensional laser scanning-based method for identifying rock discontinuities

Hu Shengming[1,2*], Gao Jianglin[1*], Hu liang[2], Dai Zhiguang[2], Chen Fang[1]

[1] Jiangxi Research Center on Hydraulic Structures, Jiangxi Academy of Water Science and Engineering, Nanchang 330029, China;
[2] National and Provincial Joint Engineering Laboratory for the Hydraulic Engineering Safety and Efficient Utilization of Water Resources of Poyang Lake Basin, Nanchang Institute of Technology, Nanchang, Jiangxi 330099, China
* Correspondence: Hu Shengming (2012994352@nit.edu.cn); Gao Jianglin (gaojianglin@163.com)

Abstract: Manual measurement of rock discontinuities is time-consuming and subjective according to the experience of the surveyor. This work proposes a three-dimensional laser scanning-based method for the semi-automatic identification of rock discontinuities. Multisite cloud scanning is performed with real-time kinematic (RTK)-assisted orientation to estimate the rock fracturing degree; then, discontinuity orientations are extracted with the man–machine interactive method or automatic method. The proposed method was applied to actual examples to illustrate its accuracy at identifying rock discontinuities. The sensitivity of the identification accuracy to different parameters was investigated.

Keywords: three-dimensional laser scanning; rock discontinuity; rock fracture; rock joint; discontinuity orientation.

1 Introduction

Discontinuities is a general term for describing planes of mechanical weakness formed by the action of tectonic stress, rock folds, and fractures in a rock mass; they include most joints, weak bedding planes, weakness zones, and faults (Ulusay, 2015; Tang et al., 2016, 2017, 2018; Idrees et al., 2018). The presence of discontinuities gives a rock mass the distinct characteristics of anisotropy and heterogeneity; they reduce the integrity and overall strength of the rock mass and increase its deformation (Wen et al., 2020). Accurately studying and collecting spatial and geometric information on rock discontinuities is of great significance for the stability analysis and evaluation of rock masses. Conventionally, discontinuities are measured manually with a geological compass or clinometer in the field and recorded in a survey notebook. Such a method tends to produce errors, and the accuracy strongly relies on the surveyor's experience (Assali et al., 2014; Huang et al., 2016, 2019, 2020a, 2020b; Idrees et al., 2018). The development of three-dimensional laser scanning (3D-LS) technology has led to great advances in research on rock discontinuities (Tomás et al., 2018; Hu et al., 2019c, 2020b; Xu et al., 2020). However, using 3D-LS technology to identify rock discontinuities accurately and efficiently for geological applications is difficult (Cinar et al., 2017; Riquelme et al., 2018).

The extraction of rock discontinuities with 3D-LS generally has two steps: (1) detecting discontinuities and extracting geometric parameters and (2) registering and

 doi:10.20944/preprints202104.0641.v1

georeferencing multisite cloud data (Hu et al., 2019b; Pagano et al., 2020). Acquiring high-quality 3D-LS point cloud data and preprocessing the point cloud are indispensable requirements. Because of the unique geometric characteristics of a rock mass (e.g., discontinuities with different orientations, irregular shapes, and different roughnesses) (Hu et al., 2019b), there is an urgent need to improve the registration and georeferencing of multisite cloud data. Geological engineers tend to simplify the complex procedures of both registration and georeferencing for rock mass discontinuity analysis by using a single scan. Hu et al. (2019a) introduced an automatic 3D registration method for rock mass point clouds. Hu et al. (2020a) also introduced a method for detecting discontinuities from 3D rock mass point clouds.

There is widespread interest in using intelligent algorithms to detect discontinuities and extract parameters automatically or semi-automatically (Chen et al. 2017). Riquelme et al. (2014) proposed identifying flat surfaces of outcroppings by the user-supervised removal of noisy points through the creation of a co-planarity test, semi-automatic identification of discontinuity sets through kernel density estimation, and automatic extraction of single discontinuities through a density-based clustering algorithm. Chen et al. (2016) proposed extracting discontinuity orientations automatically by grouping discontinuity sets with an improved K-means clustering method and fitting discontinuity planes by using the random sample consensus method. Guo et al. (2017) proposed a semi-automatic extraction method for rock mass discontinuities based on the firefly and fuzzy c-means algorithms. Ge et al. (2018) proposed using a modified region-growing algorithm to measure automatically the geometric properties of discontinuities from a point cloud. Han et al. (2018) presented a four-step approach to extracting rock mass discontinuities: organizing point cloud data with the quadtree–octree index method, calculating normal vectors by using locally triangulated irregular networks and eight neighborhood areas, double-clustering based on the quadtree–octree index and calculated normal vectors, and checking the results with an extended random sample consensus algorithm. Gomes et al. (2020) proposed an algorithm for detecting and estimating the orientation of planar structures.

Great advances have been made in the automatic or semi-automatic extraction of rock discontinuities for registration and georeferencing (Umili et al. 2020; Kong et al. 2020). However, little consideration has been given to improving the extraction accuracy and efficiency for the orientation results. In addition, a suitable extraction method that considers the development degree of rock discontinuities has not been developed. In this study, a 3D-LS-based method was developed for the rapid registration and orientation of multisite cloud data to automatically or semi-automatically identify rock discontinuities. A series of experiments was performed on a rock specimen to verify the accuracy and effectiveness of the proposed method. The proposed method was applied to a highway rock slope. Finally, Discontinuity Set Extractor (DSE) was used to perform a comprehensive sensitivity analysis on different parameters for the automatic extraction of multiple discontinuities in both the rock specimen and the highway rock slope.

2 Methodology

Preprints (www.preprints.org) | NOT PEER-REVIEWED | Posted: 23 April 2021 doi:10.20944/preprints202104.0641.v1

The aim of the proposed method is to achieve the rapid registration and orientation of multisite cloud data and to identify rock discontinuities with high accuracy and efficiency. As shown in Fig. 1, there are four main steps: multisite cloud scanning with real-time kinematic (RTK)-assisted orientation, registration of the multisite cloud data with the iterative closest point (ICP) algorithm, estimation of the development degree of rock discontinuities, and determination of the proper extraction method for spatial orientations of the rock discontinuities. The extraction method can be either man–machine interactive or automatic.

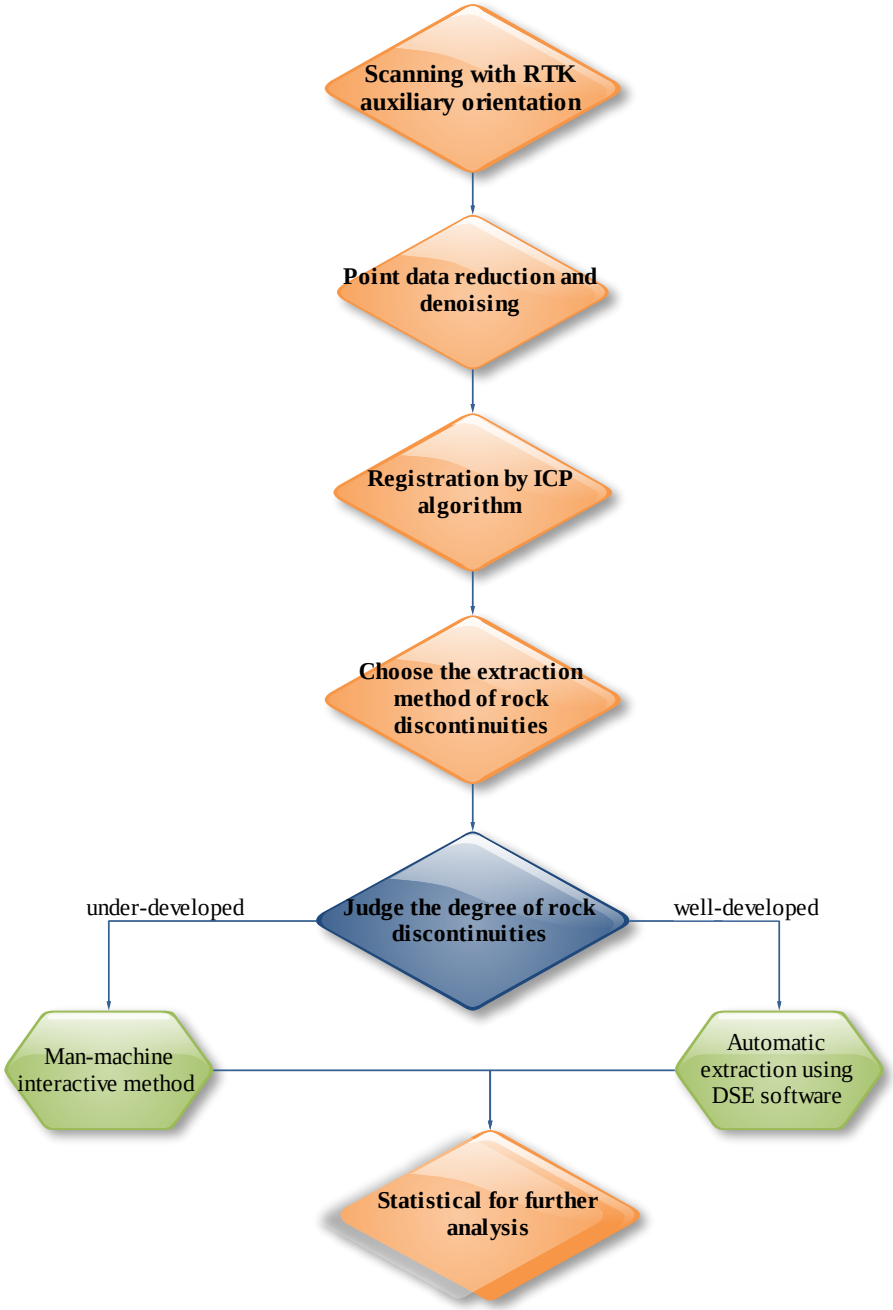

Fig. 1 Flowchart of the proposed methodology

2.1 Internal coordinate system of the 3D-LS system

Preprints (www.preprints.org) | NOT PEER-REVIEWED | Posted: 23 April 2021 doi:10.20944/preprints202104.0641.v1

With 3D-LS, a narrow-beam laser pulse is emitted by a built-in emitter that scans the target object through two rapidly rotating mirrors. The distance to the target object is calculated by measuring the time for a laser beam to bounce back from the object's surface. The relative angle of the pulse is measured with an encoder, which allows the true 3D coordinates to be calculated. As shown in Fig. 2, the center of the scanner is set as the origin of the coordinate system, so the 3D laser point coordinates can be expressed as follows:

$$\begin{cases} X = S\cos\theta\cos\alpha \\ Y = S\cos\theta\sin\alpha \\ Z = S\sin\theta \end{cases} \tag{1}$$

where α is the 3D laser transverse scanning angle, θ is the longitudinal scanning angle, and S is the scanning distance.

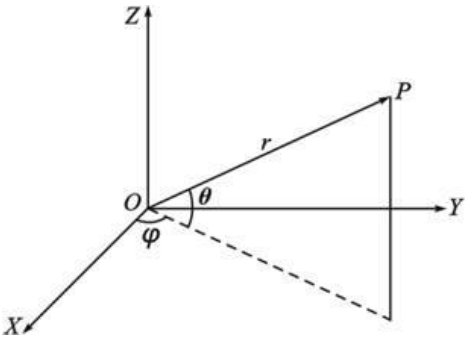

Fig. 2 Internal coordinate system of the 3D-LS system. The origin (0, 0, 0) is at the center of the scanner

2.2 Multisite cloud scanning based on RTK-assisted orientation

For RTK assistance with the orientation, the coordinates of the lofting station are obtained before scanning. At least two stations are needed to obtain the spatial orientations and ensure the accurate coordinate transformation of point cloud data from multiple stations. For the point cloud splicing, the true coordinates of each test site that are collected by the RTK instrument are imported to obtain the initial splicing position, rough splicing, and geographic orientation.

2.3 Registration of multisite cloud based on ICP algorithm

The ICP algorithm was proposed by Besl and McKay (1992), and it is among the most efficient methods for registering multisite cloud data. First, planar feature points are extracted from the spatial indices established for the multisite cloud data. Then, the minimum distance is calculated in Euclidean space according to the corresponding points within the search radius. Next, the median error is calculated for the minimum distance between the corresponding points. Finally, the spatial coordinates are transformed according to the determined corresponding points. If A_i and A_i' are the corresponding points of two point cloud sets, the coordinate transformation between point clouds in different coordinate systems is given by

Preprints (www.preprints.org) | NOT PEER-REVIEWED | Posted: 23 April 2021 doi:10.20944/preprints202104.0641.v1

$$A_i^{'} = RA_i + t \tag{2}$$

$$A_i = [x_i, y_i, z_i]^T \tag{3}$$

$$A_i^{'} = [x_i^{'}, y_i^{'}, z_i^{'}]^T \tag{4}$$

The above equations show that six parameters need to be solved for the rigid transformation matrix: α, β, γ, t_x, t_y, and t_z. In addition, at least three corresponding points that are not on a line have to be chosen in the coinciding area of point clouds. Then, six linear equations can be established to solve the parameters of the rigid transformation matrix.

Let A_i and $A_i^{'}$ be the corresponding points in the overlapping area of two point cloud sets. To minimize the error between the two sets, the least squares method is adopted to calculate the minimum error square, optimal matching function, optimal rotation matrix, and translational vector. The following objective function can be derived:

$$E(R,t) = \frac{1}{n}\sum_{i=1}^{n}\left\|A_i^{'} - (RA_i + t)\right\|^2 \tag{5}$$

where $E(R,t)$ is the mean square error of the corresponding point sets, A_i and $A_i^{'}$ (i =1, 2, 3…n) are the corresponding points, R is the rotation matrix, and t is the translational vector.

After the coordinate transformation, the corresponding points within the radius are searched iteratively. The error for the minimum distance between corresponding points is calculated iteratively until the required stitching accuracy is achieved.

2.4 Man–machine interactive extraction of orientations

The man–machine interactive extraction method is recommended for extracting discontinuities in the rock mass that are difficult to observe.

2.4.1 Preprocessing of point clouds

The raw data are reduced to select the region of interest (ROI). Redundant point cloud data are deleted after registration and georeferencing. Then, a denoising procedure is performed to reduce noise.

2.4.2 Calculation of the normal vectors

If the point cloud data of the same rock discontinuities can be fitted on a plane, then the fitted plane can be expressed as

$$Z = A + Bx + Cy \tag{6}$$

$$\begin{bmatrix} n & \sum_{i=1}^{n} x_i & \sum_{i=1}^{n} y_i \\ \sum_{i=1}^{n} x_i & \sum_{i=1}^{n} x_i^2 & \sum_{i=1}^{n} x_i y_i \\ \sum_{i=1}^{n} y_i & \sum_{i=1}^{n} x_i y_i & \sum_{i=1}^{n} y_i^2 \end{bmatrix} \cdot \begin{bmatrix} A \\ B \\ C \end{bmatrix} = \begin{bmatrix} \sum_{i=1}^{n} z_i \\ \sum_{i=1}^{n} x_i z_i \\ \sum_{i=1}^{n} y_i z_i \end{bmatrix} \tag{7}$$

where n is the number of points captured from the surface and (x_i, y_i, z_i) are coordinates of the captured points (i = 1, 2, …, n).

Preprints (www.preprints.org) | NOT PEER-REVIEWED | Posted: 23 April 2021 doi:10.20944/preprints202104.0641.v1

Multiple regression analysis can be carried out on Eq. (7) by using the least squares method in MATLAB to calculate the coefficients A, B, and C. The unit normal vector $\bar{n} = \{n_x, n_y, n_z\}$ can be obtained after normalization.

2.4.3 Calculation of the spatial orientation

The geological coordinate system is normally adopted for determining the spatial orientation of rock discontinuities. The dip direction is specified from 0° (i.e., north; equivalent to the Y-axis) to 360° and increases clockwise. The dip angle is specified from 0° to 90°, and the Z-axis is in the positive direction. The spatial orientation is calculated as follows.

2.4.3.1 Dip direction

$$\theta = \tan^{-1}\left(\frac{n_x}{n_y}\right) + Q \tag{8}$$

where n_x and n_y are the coefficients in the X and Y directions, respectively, for the unit normal vector and Q is the coefficient depending on the quadrant.

If $n_x \geq 0$ and $n_y \geq 0$, then $Q = 0°$.

If $n_x < 0$ and $n_y > 0$, then $Q = 360°$.

Otherwise, if $n_x < 0$ and $n_y < 0$, or $n_x > 0$ and $n_y < 0$, then $Q = 180°$.

2.4.3.2 Dip angle

$$\delta = 90° - \tan^{-1}\left(\frac{\mathrm{sgn}(n_z) n_z}{\sqrt{n_x^2 + n_y^2}}\right) \tag{9}$$

where n_x, n_y and n_z are the coefficients in the X, Y, and Z directions, respectively, for the unit normal vector.

2.5 Automatic extraction of multiple discontinuities with DSE

Considering that most rock slopes contain multiple sets of rock discontinuities, extracting the discontinuities with the man–machine interactive extraction method will be time-consuming. In addition, the results are easily affected by subjective factors. In this case, automatic and semi-automatic extraction methods are recommended. DSE is an open-source software program in MATLAB developed by Riquelme (2014) that can be used to extract discontinuity sets automatically from the 3D point cloud of a rock mass. The main steps are as follows:

(1) Calculate the local curvature:

Nearest neighbor search: After the point cloud file is imported, the normal vector is calculated by principal component analysis (PCA). Then, the number of nearest neighbors (*knn*) is searched for every point.

Co-planarity test: PCA is used to test the co-planarity test. Plane adjustment and calculation of the normal vector: After all subsets of coplanar points have been found, PCA is used to calculate the best-fitting adjustment plane.

(2) Analyze the statistical distribution of the poles of the normal vectors:

Density estimation: The non-parametric function of the poles is calculated in a stereonet by using kernel density estimation.

Automatic identification of rock discontinuities: Because of reading errors and singular points of curved surfaces that imply pole dispersion, only a few of the local maximums are principal poles. Automatic set identification mainly comprises calculating the principal poles and assigning poles.

Preprints (www.preprints.org) | NOT PEER-REVIEWED | Posted: 23 April 2021 doi:10.20944/preprints202104.0641.v1

(3) Cluster analysis:

The clustering process is the final operation that can affect the results. The density-based scan algorithm with noise is employed to classify the point clouds. Then, PCA is used to define the planes of these discontinuities mathematically.

3 Experimental tests

3.1 Test specimen and instrumentation

Fig. 3(a) shows the rock specimen used for the scanning test. The specimen was excavated from a fault zone at the site of a pumped storage power station in Jingan County, Jiangxi Province. This specimen comprised medium-grained granite and had an irregular shape with a volume of approximately 4 m^3. It was light red in color, slightly weathered, massive, and blocky with a striated surface. Fig. 3(b) shows the 3D terrestrial scanner Riegl VZ-1000 that was utilized to scan the test specimen.

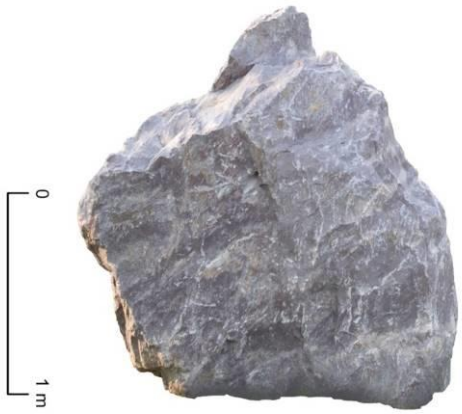

(a) Photograph of the scanning test specimen

(b) 3D terrestrial scanner of Riegl VZ-1000

Fig. 3 Experimental specimen and scanning instrument

3.2 Experimental scheme and design

To verify the accuracy and effectiveness of the proposed method at extracting orientations of rock discontinuities, two groups of experiments were designed: scanning and extracting a single discontinuity and scanning and automatically extracting multiple discontinuities. A manual investigation method was performed to provide a baseline for the extraction accuracy.

3.2.1 Scanning and extraction tests of a single discontinuity

The scanning and extraction tests of a single discontinuity were performed to verify the accuracy of the structural plane test results extracted with the RTK-assisted orientation and ICP registration methods and to analyze the influence of different factors during the scanning process on the spatial orientation of the rock discontinuities. A rock discontinuity plane with good integrity in the test specimen was

Preprints (www.preprints.org) | NOT PEER-REVIEWED | Posted: 23 April 2021 doi:10.20944/preprints202104.0641.v1

selected. The plane was located in the facing direction, as shown in Fig. 3. To analyze the impact of the scanning distance and angular resolution on the orientation results, the scanning distance was set to 5, 10, 20, 40, and 60 m. Different sites on the specimen were tested along a straight line to keep the scanning incident angle fixed, whereas the angular resolution of each site was set to 0.06° or 0.02°.

3.2.2 Scanning and automatic extraction tests of multiple discontinuities

The scanning and automatic extraction tests of multiple discontinuities were performed to verify the automatic extraction with DSE and to analyze and optimize the main influencing factors. In total, five scans were performed at a scanning distance of 6–8 m to acquire a complete 3D point cloud model of the rock specimen. Fig. 4 shows the layout of the scanning sites. DSE was used for the automatic extraction of multiple discontinuity sets.

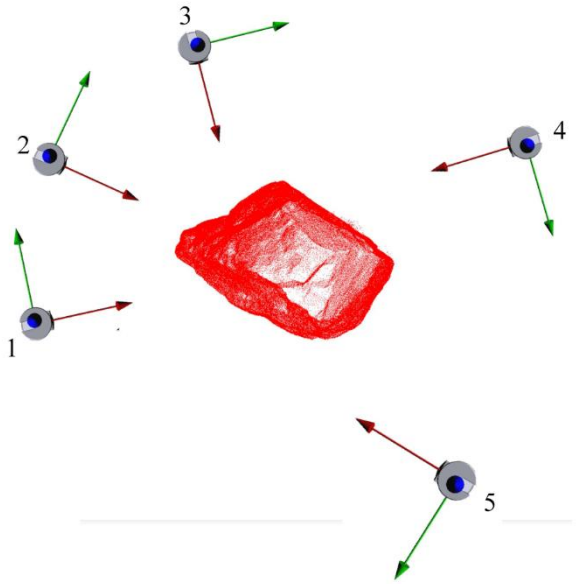

Fig. 4 Layout of the multiple scans

4 Experimental results

4.1 Extraction results for a single discontinuity

4.1.1 Accuracy of the extraction results

Table 1 presents the calculated results without RTK-assisted orientation for the scanning point data of each station sampled at an angular resolution of 0.02°. The dip angle remained almost the same among stations. However, the dip direction varied significantly with a range of 95°. Table 2 presents the calculated results with RTK-assisted orientation and ICP registration at an angular resolution of 0.02°. The dip angle and dip direction remained almost the same among different stations. For this discontinuity set, the manual method was also utilized; 15 relatively flat small planes that were evenly distributed on the surface of the discontinuity were investigated with a geologic compass.

Preprints (www.preprints.org) | NOT PEER-REVIEWED | Posted: 23 April 2021 doi:10.20944/preprints202104.0641.v1

Fig. 5 shows the orientation of this discontinuity set that was obtained with the stereo polar density projection: 324.8°∠81°.

Table 1: Calculated orientation results without RTK-assisted orientation (0.02°)

Distance	Normal vectors			Dip direction	Dip angle
	n_x	n_y	n_z	(°)	(°)
~5 m	0.3603	0.9294	-0.0803	201	85
~10 m	0.5071	0.8587	-0.0742	211	86
~20 m	0.4534	0.8882	-0.0737	207	86
~40 m	0.9976	-0.0075	-0.0688	270	86
~60 m	-0.0945	0.9932	-0.0679	175	86

Table 2: Calculated orientation results after RTK-assisted orientation and ICP registration (0.02°)

Distance	Normal vectors			Dip direction	Dip angle
	n_x	n_y	n_z	(°)	(°)
~5 m	0.537	-0.8408	-0.0684	327	86
~10 m	0.5343	-0.8422	-0.0725	328	86
~20 m	0.5336	-0.8426	-0.0728	328	86
~40 m	0.5339	-0.843	-0.0665	328	86
~60 m	0.5323	-0.8433	-0.0744	328	86

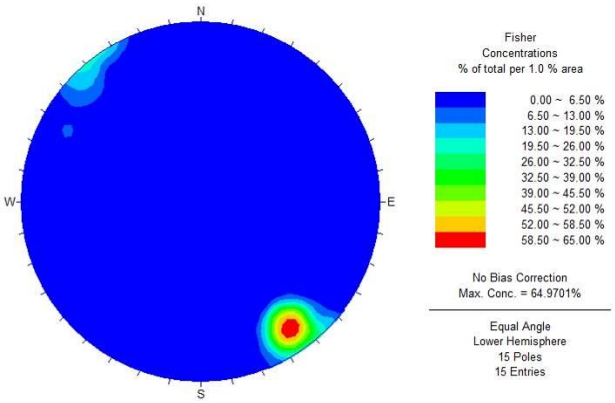

Fig. 5 Stereo polar density plot of the manual investigation

The results with and without RTK-assisted orientation and ICP registration demonstrated that these techniques can help effectively extract the spatial orientation of rock discontinuities. Furthermore, the results with 3D-LS and the manual method indicated that the dip direction and angle had biases of approximately 4° and 5°, respectively. These were attributed to the limited acquisition size of the geological

Preprints (www.preprints.org) | NOT PEER-REVIEWED | Posted: 23 April 2021 doi:10.20944/preprints202104.0641.v1

compass. In summary, the proposed method can extract the spatial orientation of a discontinuity reliably and accurately.

4.1.2 Influences of the angular resolution and scanning distance

To analyze the influence of the angular resolution on the extraction results, additional experiments were performed at an angular resolution of 0.06°. Table 3 presents the calculated results. Table 4 lists the differences in orientation at different angular resolutions; both the dip direction and the angle were very consistent with different angular resolutions. This indicates that the angular resolution of the sampling has a slight effect on the orientation results. Table 5 lists the orientation differences with different scanning distances. Both the dip direction and the angle remained consistent at different scanning distances. Thus, the scanning distance has little effect on the orientation results.

Table 3: Calculated orientation results after registration/georeferencing (0.06°)

Distance	Normal vectors			Dip direction (°)	Dip angle (°)
	n_x	n_y	n_z		
~5 m	0.5342	-0.8419	-0.077	328	86
~10 m	0.5341	-0.8424	-0.0706	328	86
~20 m	0.5327	-0.8432	-0.0723	328	86
~40 m	0.5341	-0.8427	-0.0686	328	86
~60 m	0.5339	-0.8425	-0.072	328	86

Table 4: Statistical results for the orientation differences with different resolutions

Registration	~5 m		~10 m		~20 m		~40 m		~60 m	
	$\Delta\lvert DD\rvert$	$\Delta\lvert DA\rvert$	$\Delta\lvert DD\rvert$	$\Delta\lvert DA\rvert$	$\Delta\lvert DD\rvert$	$\Delta\lvert DA\rvert$	$\Delta\lvert DD\rvert$	$\Delta\lvert DA\rvert$	$\Delta\lvert DD\rvert$	$\Delta\lvert DA\rvert$
RTK-assisted orientation & ICP registration	1	0	0	0	0	0	0	0	0	0

Note: DD = dip direction, DA = dip angle

Table 5: Statistical results for the orientation differences with different distances (0.02°)

Registration	Dip direction (°)				Dip angle (°)			
	Max.	Min.	Mean	Stand. dev.	Max.	Min.	Mean	Stand. dev.
RTK-assisted orientation	328	327	327.8	0.45	86	86	86	0.00

Preprints (www.preprints.org) | NOT PEER-REVIEWED | Posted: 23 April 2021 doi:10.20944/preprints202104.0641.v1

& ICP registration	

4.2 Extraction results for multiple discontinuities

4.2.1 Accuracy of the extraction results

Fig. 6 shows the automatic extraction results for the orientations of multiple discontinuities at the recommended values of *knn* = 30, six bin levels, and a minimum angle of 30°. Fig. 6(a) shows the loaded 3D point cloud data of the rock specimen, and Fig. 6(b) shows the stereographic projection results of the normal vector poles without the hue–saturation–value (HSV) color map. Fig. 6(c) shows the 3D point cloud data of the rock specimen, and Fig. 6(d) shows the stereographic projection of the normal vector poles, both with the HSV color map. Fig. 6(e) shows the stereonet of the density of the normal vector poles and the corresponding planes. After poles were assigned by adjustment of the cone filter threshold and the statistical distribution of the normal vector poles was analyzed, the main spatial orientations of joints were extracted, as listed in Table 6.

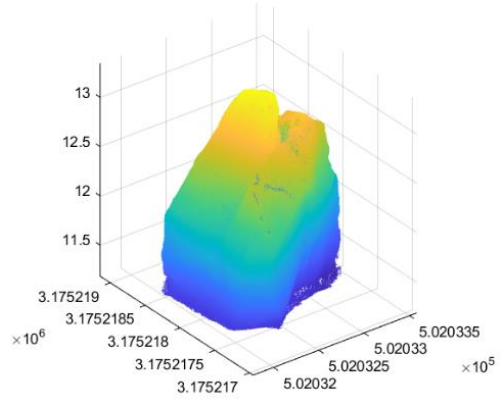

(a) Loaded 3D point cloud data

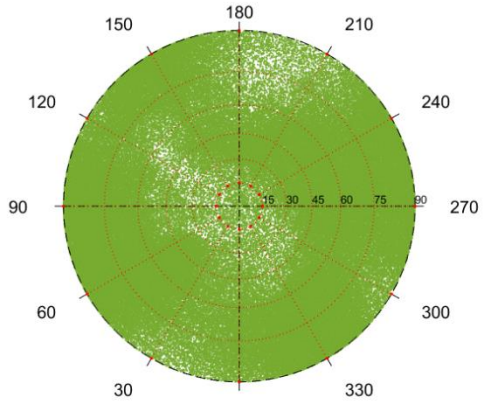

(b) Stereographic projection of the normal vector poles without the HSV color map

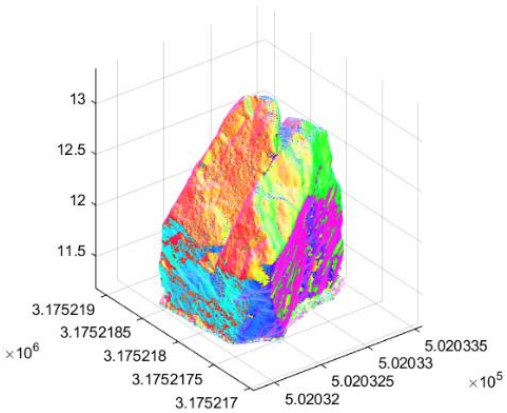

(c) 3D point cloud with the HSV color map

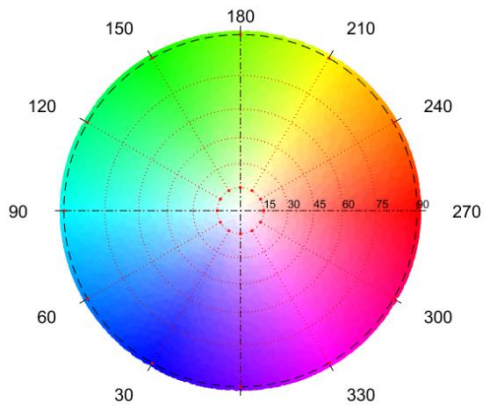

(d) Stereographic projection of the normal

Preprints (www.preprints.org) | NOT PEER-REVIEWED | Posted: 23 April 2021 doi:10.20944/preprints202104.0641.v1

vector poles with the HSV color map

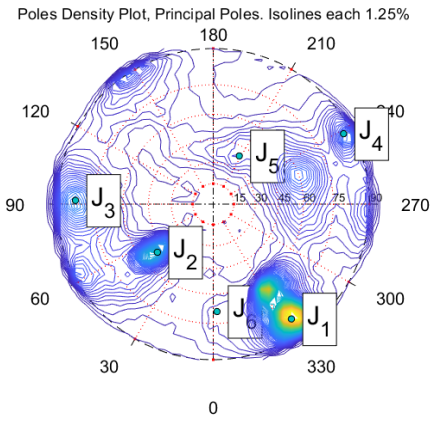

(e) Stereonet of the density of the normal vector's poles and its corresponding planes

Fig. 6 Automatic extraction results of discontinuity sets

Table 6: Automatically extracted discontinuity sets of the rock specimen

Discontinuity sets	Dip direction (°)	Dip angle (°)	Density(%)
J1	323.4	85.2	4.9
J2	49.1	50.6	2.3
J3	248.7	60.9	1.9
J4	88.5	85.8	1.7
J5	55.9	83.4	0.6
J6	204.5	32.0	0.4

To provide a baseline for evaluating the accuracy of the automatic extraction results, different groups of discontinuity sets were also measured manually. In total, 45 relatively flat small planes that were well distributed on the surface of the rock specimen were investigated with a geologic compass. As shown in Fig. 7, the orientations of the main discontinuity sets were obtained by using stereo polar density projection: 325°∠88°, 88°∠84°, and 63°∠88°.

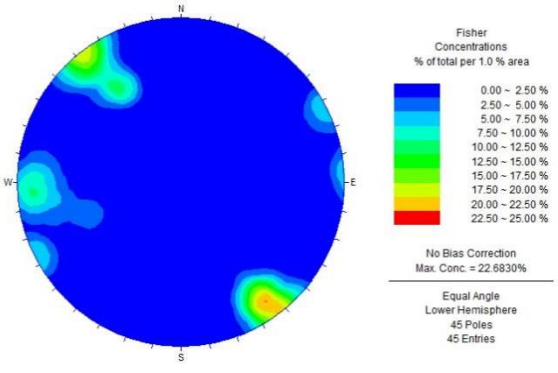

Fig. 7 Stereo polar density plot of the manual investigation

Preprints (www.preprints.org) | NOT PEER-REVIEWED | Posted: 23 April 2021 doi:10.20944/preprints202104.0641.v1

A comparison of the orientation results extracted automatically by DSE and extracted manually shows that both methods identified three groups of rock discontinuity sets: J1, J4, and J5. The biases for the dip direction and angle were respectively 1.6° and 2.8° for J1, 0.5° and 1.8° for J4, and 7.1° and 4.6° for J5. The biases for J1 and J4 are acceptable, but those for J5 are relatively large. Furthermore, the manual extraction ignored two groups of discontinuity sets: J2 and J3. These results indicate that the proposed method can automatically extract rock discontinuity sets accurately and completely, and it can effectively make up for the shortcomings of the manual approach. For example, the orientation results are easily affected by human factors, or some discontinuity sets may be ignored.

4.2.2 Influence of extraction parameters

A comprehensive sensitivity analysis was performed to identify the optimal values of the parameters for the automatic extraction method with this particular rock specimen. The number of neighbors (*knn*) is an important parameter for the co-planarity test calibration and pole dispersion in the stereoplot. Bin levels characterize the width of the kernels, and the minimum angle is the angle between the associated normal vector and the assigned normal vector on the principal plane; these are important for the density and principal pole extraction processes. Thus, *knn*, bin levels, and minimum angle were selected as the main extraction parameters for the sensitivity analysis.

4.2.2.1 Influence of *knn*

Different *knn* values were considered to evaluate the influence of *knn* on the accuracy of the automatically extracted orientations. Four groups of main discontinuity sets were automatically extracted with *knn* = 15, 30, 45, 60, 75, and 90. Table 7 lists the angular differences between the extracted orientations with different *knn* values. For J1, the biases for the mean dip direction, mean dip angle, and mean point cloud density between the *knn* ranges of 15–90 and 15–60 were 0.1, 0.4, and 0.2, respectively. The biases for the corresponding standard deviations were 0.1, 0.4, and 0.1, respectively. For J2, the biases of the mean dip direction, mean dip angle, and mean point cloud density were 0.7, 0.2, and 0.2, respectively. The biases for the corresponding standard deviations were 0.3, 0.1, and 0.0, respectively. For J3, the biases for the mean dip direction, mean dip angle, and mean point cloud density were 0.4, 0.2, and 0.1, respectively. The biases for the corresponding standard deviations were 0.4, 0.3, and 0.1, respectively. For J4, the biases for the mean dip direction, mean dip angle, and mean point cloud density were 0.5, 0.5, and 0.1, respectively. The biases for the corresponding standard deviations were 0.2, 0.6, and 0.0, respectively. For the underdeveloped discontinuities of this rock specimen, the automatically extracted orientations were consistent with different *knn* values; the dip direction, dip angle, and point cloud density varied only slightly between the *knn* ranges of 15–90 and 15–60.

Preprints (www.preprints.org) | NOT PEER-REVIEWED | Posted: 23 April 2021 doi:10.20944/preprints202104.0641.v1

Table 7: Mean values and standard deviation of the main discontinuity sets for different ranges of *knn*

Range		15–90		15–60	
Discontinuity sets	Parameters	Mean values	Stand. Dev.	Mean values	Stand. Dev.
J1	DD (°)	323.5	0.28	323.6	0.34
	DA (°)	84.4	1.74	84.1	2.13
	Density	4.5	0.71	4.3	0.79
J2	DD (°)	250.1	2.26	250.8	2.54
	DA (°)	60.5	0.68	60.2	0.76
	Density	1.6	0.42	1.4	0.41
J3	DD (°)	49.9	1.91	50.3	2.34
	DA (°)	50.1	1.15	49.9	1.40
	Density	2.0	0.46	1.9	0.54
J4	DD (°)	89.5	1.58	90.0	1.77
	DA (°)	84.7	2.51	84.2	3.07
	Density	1.5	0.42	1.4	0.46

Note: DD = dip direction, DA = dip angle, Density = point cloud density

4.2.2.2 Influence of bin levels

Table 8 lists the dip direction, dip angle, and point cloud density of the main discontinuities automatically extracted with different bin levels. At 6–12 bin levels, four main discontinuity sets were automatically extracted. However, only three main discontinuity sets were automatically determined with four bin levels. For J1, the mean dip direction and mean dip angle with 4–12 bin levels were 325.9° and 81.3°, respectively, and the corresponding standard deviations were 0.9 and 1.2, respectively. For J2, the mean dip direction and mean dip angle with 6–12 bin levels were 49.3° and 52.5°, respectively, and the corresponding standard deviations were 0.3 and 1.3, respectively. However, the dip direction and dip angle sharply increased with biases of 9.8° and 8.0°, respectively, at four bin levels. For J3, the mean dip direction and mean dip angle with 6–12 bin levels were 91.0° and 82.0°, respectively, and the corresponding standard deviations were 0.4 and 0.5, respectively. However, the dip direction and dip angle sharply increased with biases of 7.4° and 2.3°, respectively, at four bin levels. For J4, the mean dip direction and mean dip angle with 6–12 bin levels were 242.2° and 86.2°, respectively, and the corresponding standard deviations were 0.5 and 0.5, respectively. The point cloud density increased with the bin level for all four discontinuity sets.

Table 8: Main discontinuities automatically extracted with different bin levels

Note: DD = dip direction, DA = dip angle, Density = point cloud density

4.2.2.3 Influence of the minimum angle

The three main discontinuity sets that were automatically extracted had a consistent dip direction, dip angle, and point cloud density within a minimum angle range of 15°–

Preprints (www.preprints.org) | NOT PEER-REVIEWED | Posted: 23 April 2021 doi:10.20944/preprints202104.0641.v1

35°. However, the dip direction, dip angle, and point cloud density of other discontinuity sets greatly differed with the minimum angle. At minimum angles of 10° and 15°, the same discontinuity set may be divided into two groups (e.g., 325.9°∠83.4° and 326.9°∠66.3°).

5 Example application to a highway slope

As an example, the proposed method was applied to a rock slope excavated from limestone in the Dean section of the reconstruction and extension project for the Nanchang–Jiujiang Expressway, as shown in Figs. 8 and 9.

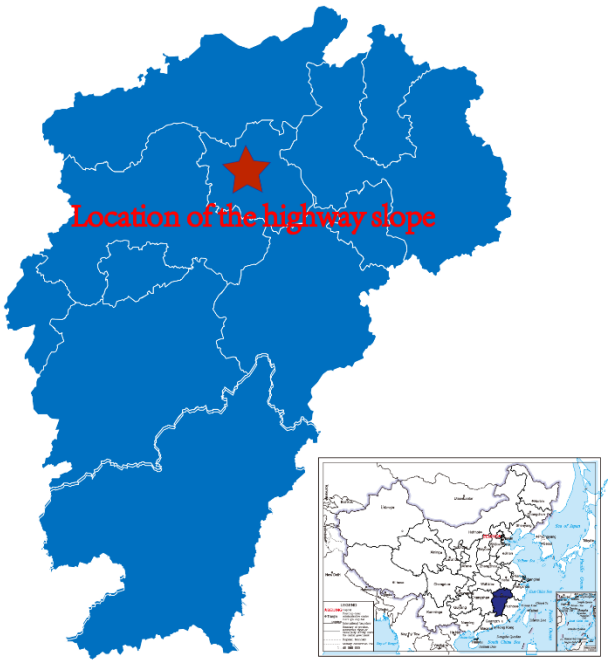

Fig. 8 Location of the rock slope along the Nanchang–Jiujiang Expressway

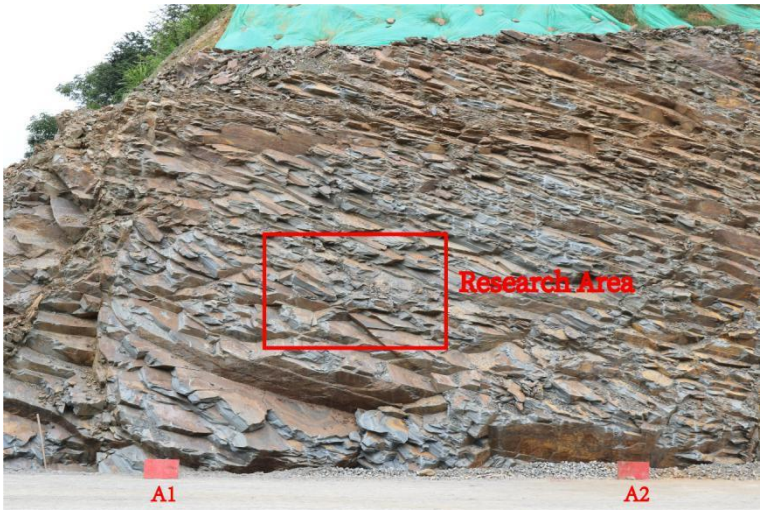

Fig. 9 Highway rock slope used in this study. The red rectangle represents the selected area for automatic extraction; two flat wooden boards were placed at the foot of the slope for reference

Preprints (www.preprints.org) | NOT PEER-REVIEWED | Posted: 23 April 2021 doi:10.20944/preprints202104.0641.v1

5.1 Extraction of orientations of the free slope surface and discontinuities

During the scanning process, two flat wooden boards were placed at the foot of the slope as a reference (A1 on the left and A2 on the right, as shown in Fig. 9). The spatial orientations of these two flat wooden boards were measured manually with a geological compass and with the proposed method. Table 9 compares the results. The results of the manual extraction and proposed method were quite consistent. The spatial orientation of the free slope surface (S1) was also extracted with the man–machine interactive extraction method and found to be 282.4°∠55.2°. Considering that the joints of the slope are well developed, the manual and man–machine interactive extraction methods were inefficient and time-consuming.

Table 9: Spatial orientations of the two flat boards

Num.	Manual method		3D-LS method	
	Dip direction (°)	Dip angle (°)	Dip direction (°)	Dip angle (°)
A1	281.6	74.3	280.0	73.2
A2	285.2	85.1	283.8	85.2

Because an excess of poles in the stereoplot may mask the principal orientations, analyzing a huge number of points in the same test is not recommended. Thus, only part of the representative point clouds was selected as the ROI. Fig. 10 shows the automatically extracted orientations of multiple discontinuities with the proposed method for the scanning point data of the ROI. Fig. 10(a) shows the loaded 3D point cloud data of the rock specimen, and Fig. 10(b) shows the stereographic projection results of the normal vector poles without the HSV color map. Fig. 10(c) shows the 3D point cloud data of the rock specimen and Fig. 10(d) shows the stereographic projection of the normal vector poles, both with the HSV color map. Fig. 10(e) shows the stereonet of the density of the normal vector poles and the corresponding planes. After poles were assigned by adjustment of the cone filter threshold, the statistical distribution of the normal vector poles was analyzed. Table 10 lists the main spatial orientations of the joints that were extracted.

Preprints (www.preprints.org) | NOT PEER-REVIEWED | Posted: 23 April 2021 doi:10.20944/preprints202104.0641.v1

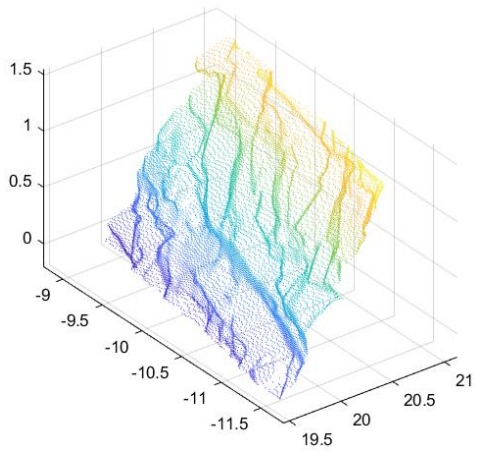

(a) Loaded 3D point cloud data of the analyzed sector

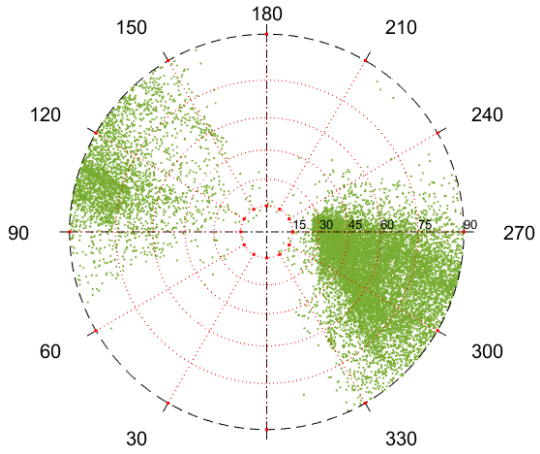

(b) Stereographic projection of the normal vector poles without the HSV color map

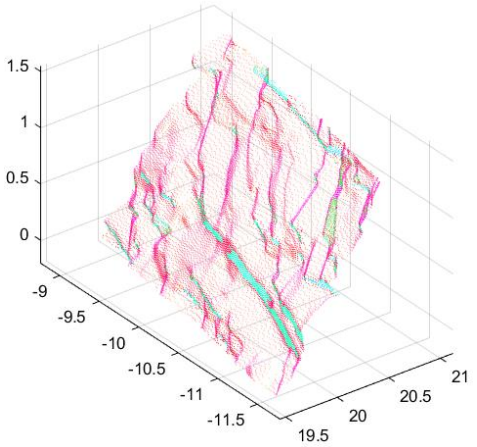

(c) 3D point cloud with the HSV color map

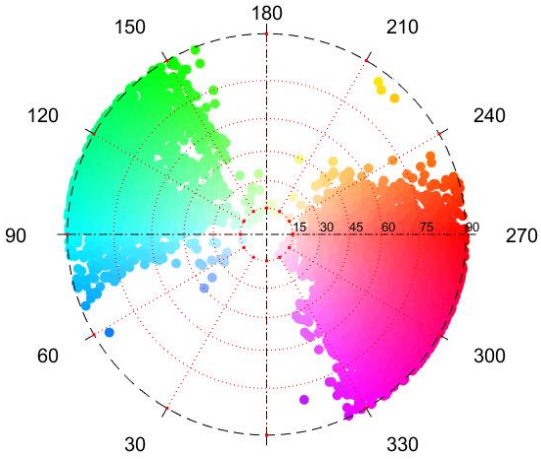

(d) Stereographic projection of the normal vector poles with the HSV color map

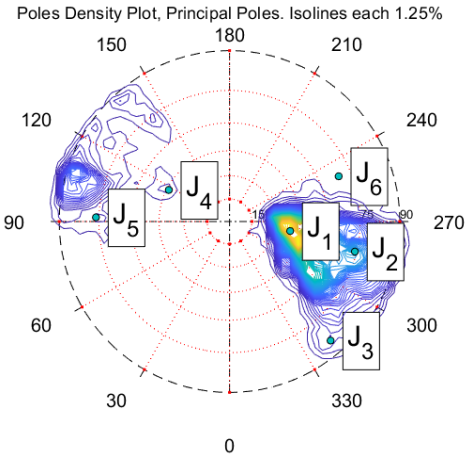

(e) Stereonet of the density of the normal vector's poles and the corresponding planes

Fig. 10. Extraction of the rock discontinuity sets

Preprints (www.preprints.org) | NOT PEER-REVIEWED | Posted: 23 April 2021 doi:10.20944/preprints202104.0641.v1

Table 10: Extracted discontinuity sets of the highway slope

Discontinuity sets	Dip direction (°)	Dip angle (°)	3D-LS Method
S1	282.4	55.2	Man-machine interactive extraction
J1	263.5	29.4	Automatic extraction by DSE
J2	301.3	55.6	Automatic extraction by DSE
J3	108.3	85.5	Automatic extraction by DSE
J4	140.7	86.2	Automatic extraction by DSE
J5	250.2	72.2	Automatic extraction by DSE

5.2 Influence of extraction parameters

A comprehensive sensitivity analysis was performed to identify the optimal values of the parameters *knn*, bin levels, and minimum angle for automatic extraction of the slope with developed joints.

5.2.1 Influence of *knn*

To evaluate the influence of *knn* on the extraction accuracy, the automatically extracted orientation results with different *knn* values (= 15, 30, 45, 60, 75, and 90) were compared. Fig. 11 shows the stereonet of the density of the normal vector poles. The morphology of the stereonet remained similar with different *knn* values. However, for the different discontinuity sets, the order of the density of the normal vector poles changed with *knn*, especially above the fourth order. Four groups of main discontinuity sets were automatically extracted with different *knn* values, and the angular differences are listed in Table 11. For J1′, the biases of the mean dip direction, mean dip angle, and mean point cloud density between the *knn* ranges of 15–90 and 15–60 were 5.3, 3.3, and 1.7, respectively. The biases of the corresponding standard deviations were 5.4, 4.9, and 0.7, respectively. For J2′, the biases of the mean dip direction, mean dip angle, and mean point cloud density were 4.5, 4.1, and 0.0, respectively. The biases of the corresponding standard deviations were 1.3, 2.0, and 0.2, respectively. For J3′, the biases of the mean dip direction, mean dip angle, and mean point cloud density were 5.8, 9.1, and 1.1, respectively. The biases of the corresponding standard deviations were 5.9, 10.7, and 1.4, respectively. For J4′, the biases of the mean dip direction, mean dip angle, and mean point cloud density were 3.0, 10.2, and 0.5, respectively. The biases of the corresponding standard deviations were 3.9, 0.5, and 0.1, respectively. Compared with the automatically extracted orientations of the rock specimen (see Section 4.2.2), the biases for the highway slope were much larger, especially at the *knn* range of 15–90. The dip direction, dip angle, and point cloud density were consistent at the *knn* range of 15–60, but these values differed significantly between the *knn* ranges of 75–90 and 15–60. This may be attributed to the well-developed joints of this highway slope.

Preprints (www.preprints.org) | NOT PEER-REVIEWED | Posted: 23 April 2021 doi:10.20944/preprints202104.0641.v1

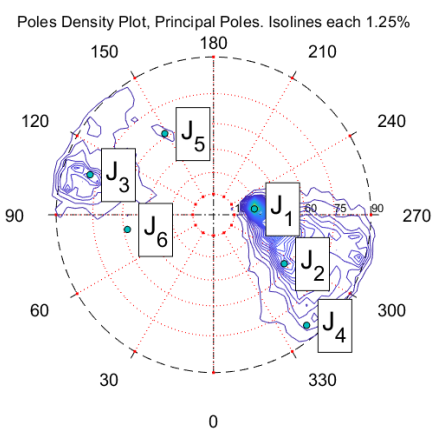

(a) *knn* = 15

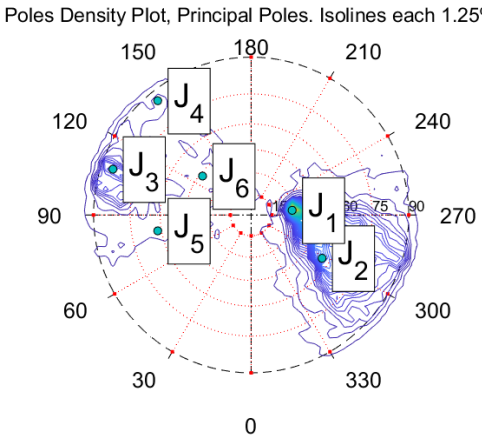

(b) *knn* = 30

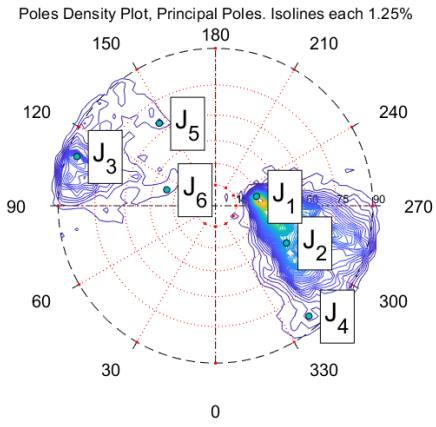

(c) *knn* = 45

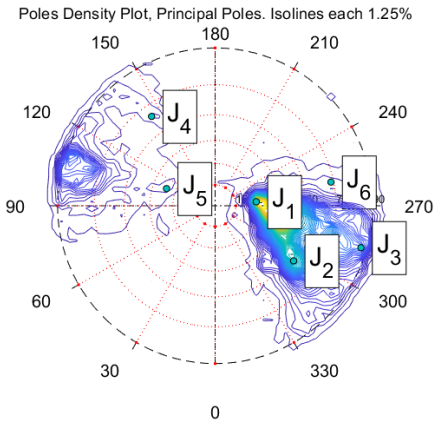

(d) *knn* = 60

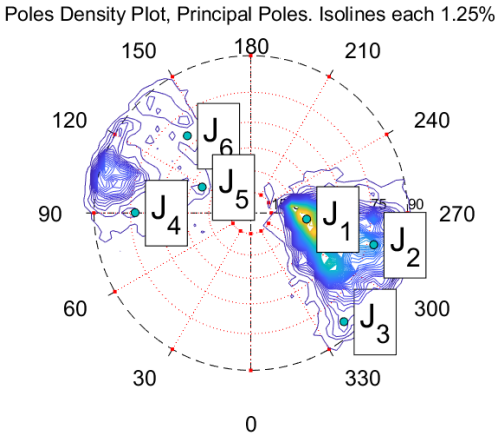

(e) *knn* = 75

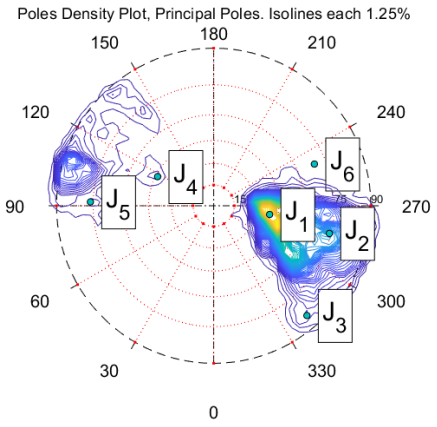

(f) *knn* = 90

Fig. 11 Stereonet of the density of the normal vector's poles

Table 11: Mean values and standard deviation of the main joint sets between different ranges of *knn*

Preprints (www.preprints.org) | NOT PEER-REVIEWED | Posted: 23 April 2021 doi:10.20944/preprints202104.0641.v1

Range		15–90		15–60	
Discontinuity sets	Parameters	Mean values	Stand. Dev.	Mean values	Stand. Dev.
J1'	DD (°)	264.5	8.49	259.9	0.23
	DA (°)	33.9	10.98	28.8	0.18
	Density	31.3	21.31	46.3	5.88
J2'	DD (°)	302.4	0.70	302.7	0.12
	DA (°)	54.3	0.86	53.8	0.05
	Density	5.1	0.91	5.5	0.22
J3'	DD (°)	100.0	0.07	100.0	0.07
	DA (°)	86.6	0.20	86.6	0.20
	Density	4.3	0.68	4.3	0.68
J4'	DD (°)	311.1	0.06	311.1	0.06
	DA (°)	87.3	0.11	87.3	0.11
	Density	1.6	0.11	1.6	0.11

Note: DD = dip direction, DA = dip angle, Density = point cloud density

5.2.2 Influence of the bin level

Table 12 lists the dip direction, dip angle, and point cloud density of the main discontinuities automatically extracted with different bin levels. At 8–12 bin levels, four discontinuity sets were automatically extracted. However, only two discontinuity sets were automatically extracted with six bin levels, and only one discontinuity set was automatically extracted with four bin levels. For J1′, the mean dip direction and mean dip angle with 6–12 bin levels were 260.8° and 29.0°, respectively, and the corresponding standard deviations were 1.8 and 0.3, respectively. However, the dip direction and dip angle sharply increased with four bin levels to reach biases of 18.7° and 24.5°, respectively. For J2′, the mean dip direction and mean dip angle with 6–12 bin levels were 302.7° and 53.8°, respectively, and the corresponding standard deviations were 0.1 and 0.0, respectively. For J3′, the mean dip direction and mean dip angle with 8–12 bin levels were 100.0° and 86.6°, respectively, and the corresponding standard deviations were 0.1 and 0.2, respectively. For J4′, the mean dip direction and mean dip angle with 8–12 bin levels were 311.1° and 87.3°, respectively, and the corresponding standard deviations were 0.1 and 0.1, respectively. The point cloud density increased with the bin level for all of the discontinuity sets.

Table 12: Main discontinuities automatically extracted with different bin levels

Discontinuity sets	Bins level	12	10	8	6	4
J1'	DD (°)	259.9	260.2	259.7	263.5	279.5
	DA (°)	28.8	29.0	28.7	29.4	53.5
	Density	50.0	49.3	39.5	14.3	3.2
J2'	DD (°)	302.7	302.7	302.9	301.3	
	DA (°)	53.8	53.8	53.9	55.6	

Preprints (www.preprints.org) | NOT PEER-REVIEWED | Posted: 23 April 2021 doi:10.20944/preprints202104.0641.v1

	Density	5.6	5.6	5.2	3.7
	DD (°)	100.1	100.1	100.0	
J3'	DA (°)	86.4	86.5	86.8	
	Density	4.8	4.5	3.5	
	DD (°)	311.2	311.1	311.2	
J4'	DA (°)	87.2	87.3	87.4	
	Density	1.6	1.6	1.4	

Note: DD = dip direction, DA = dip angle, Density = point cloud density

5.2.3 Influence of the minimum angle

For the minimum angle range of 15°–35°, three groups of discontinuity sets were automatically extracted, and the dip direction, dip angle, and point cloud density were consistent. However, the dip direction, dip angle, and point cloud density of other discontinuities were very different depending on the minimum angle.

6 Discussion

For most sites of geological disasters and their surrounding areas, no control points are prearranged. Thus, obtaining the absolute coordinates by referencing control points is difficult. Rapidly and efficiently registering the orientation of multisite cloud data at multiple sites has become a key bottleneck for the utilization of 3D-LS technology in geological applications. RTK-assisted orientation has demonstrated a good field performance because the reference stations do not need to be set during the conversion of coordinate systems and the tedious process of registering and referencing orientations is simplified, which significantly improves efficiency. In addition, ICP registration of multisite cloud data improves the registration efficiency and accuracy of the extracted spatial orientations significantly while reducing the subjectivity of manual splicing. The proposed method for using 3D-LS to extract rock discontinuities first applies RTK-assisted orientation and ICP registration of multisite cloud data. Then, the proper method for extracting the spatial orientations of rock discontinuities is determined according to the development degree. For underdeveloped discontinuities (i.e., ≤2 groups of discontinuity sets or ≤10 planes of rock discontinuities), or when the planes that need to be measured are uneven, the man–machine interactive extraction method is recommended. For well-developed discontinuities (i.e., ≥2 groups of discontinuity sets or ≥10 planes of rock discontinuities), the automatic extraction of multiple discontinuities with DSE is recommended. For the automatic extraction of multiple discontinuities with DSE, the main parameters need to be optimized. Sensitivity analysis determined that the optimal *knn*, bin levels, and minimum angle for the rock specimen in this study were 15–90, 6–12, and 20°–35°, respectively. Meanwhile, the optimal values for the highway slope were 15–60, 8–12, and 20°–35°, respectively. Thus, the recommended values for automatic extraction are *knn*, bin levels, and minimum angle of 15–60, 8–12, and 20°–35°, respectively.

7 Conclusion

A 3D-LS-based method is proposed for extracting the spatial orientation of rock discontinuities. This method involves multisite cloud scanning with RTK-assisted orientation, registration of multisite cloud data with the ICP algorithm, estimation of the fracturing degree, and determination of the proper method for extracting the spatial orientation. The extraction methods can be man–machine interactive extraction for underdeveloped discontinuities and automatic extraction with DSE for well-developed discontinuities. The accuracy and effectiveness of the proposed method were verified with both the man–machine interactive extraction method and the automatic extraction method. The scanning angle resolution and distance of 3D-LS were demonstrated to have little influence on the accuracy of the orientation extraction. The recommended values for the main extraction parameters are *knn* of 15–60, 8–12 bin levels, and a minimum angle of 20°–35°.

Acknowledgments This research was supported by the Jiangxi Provincial Key Sci entific Research Plan (No. 20203BBGL73220); Research Foundation of Education Bu reau of Jiangxi Province, China (Nos. GJJ201904 and GJJ190944); Water Science an d Technology Fund of Jiangxi Province in China (No s. 202124ZDKT15 and 2018 20ZDKT03); and Natural Science Foundation of Jiangxi Province of China (No. 20192B AB216037).

Compliance with ethical standards

Conflict of interest The authors declare that there is no conflict of interest regarding the publication of this article.

Preprints (www.preprints.org) | NOT PEER-REVIEWED | Posted: 23 April 2021 doi:10.20944/preprints202104.0641.v1

Supplementary tables

Supplementary Table S1: Automatically extracted orientations of the rock specimen with different knn values

knn level	Dip direction (°)	Dip angle (°)	Density (%)
***knn* = 90**	323.4	85.1	5.1
	49.1	50.6	2.3
	248.7	60.9	2.1
	88.5	85.8	1.9
	204.5	32.0	0.4
	149.0	45.2	0.2
***knn* = 75**	323.4	85.2	4.9
	49.1	50.6	2.3
	248.7	60.9	1.9
	88.5	85.8	1.7
	55.9	83.4	0.6
	204.5	32.0	0.4
***knn* = 60**	323.4	85.1	4.7
	49.1	50.6	2.2
	253.1	59.6	1.7
	88.5	85.8	1.6
	204.4	32.1	0.4
	295.5	62.5	0.2
***knn* = 45**	323.4	85.1	4.4
	49.2	50.5	2.0
	91.5	85.8	1.4
	253.0	59.6	1.3
	58.6	81.7	0.6
	202.4	47.3	0.4
***knn* = 30**	323.4	85.2	4.9
	49.1	50.6	2.3
	248.7	60.9	1.9
	88.5	85.8	1.7
	55.9	83.4	0.6
	204.5	32.0	0.4
***knn* = 15**	324.1	80.9	3.2
	53.8	47.8	1.1
	248.6	60.9	1.0
	91.7	79.6	0.7
	201.0	36.7	0.4
	286.9	59.6	0.3

Preprints (www.preprints.org) | NOT PEER-REVIEWED | Posted: 23 April 2021 doi:10.20944/preprints202104.0641.v1

Supplementary Table S2: Automatically extracted orientations of the rock specimen with different bin levels

Bin level	Dip direction (°)	Dip angle (°)	Density (%)
bin level = 12	326.2	80.4	4.51
	49.1	53.1	2.06
	90.7	81.7	1.30
	242.4	85.9	1.10
	248.0	56.3	1.00
	206.3	35.1	0.48
bin level = 10	326.3	80.6	4.51
	49.1	53.0	2.07
	90.7	81.8	1.29
	242.4	86.1	1.10
	248.3	56.3	1.01
	206.2	35.0	0.48
bin level = 8	326.9	80.7	4.43
	49.8	53.2	2.01
	91.2	81.7	1.26
	242.6	86.1	1.08
	237.5	56.4	0.68
	274.3	57.5	0.63
bin level = 6	325.9	83.4	3.94
	49.1	50.6	1.76
	91.6	82.8	1.19
	241.5	86.9	0.97
	208.3	38.7	0.40
	358.0	69.3	0.22
bin level = 4	324.5	81.4	2.48
	83.7	84.3	0.84
	59.0	60.5	0.77
	258.7	54.0	0.61

Preprints (www.preprints.org) | NOT PEER-REVIEWED | Posted: 23 April 2021 doi:10.20944/preprints202104.0641.v1

Supplementary Table S3: Automatically extracted orientations of the rock specimen with different minimum angles

Min. angle level	Dip direction (°)	Dip angle (°)	Density (%)
Min. angle = 35	325.9	83.4	3.9
	49.1	50.6	1.8
	91.6	82.8	1.2
	253.1	59.6	1.0
	208.3	38.7	0.4
	149.9	55.2	0.2
Min. angle = 30	325.9	83.4	3.9
	49.1	50.6	1.8
	91.6	82.8	1.2
	241.5	86.9	1.0
	208.3	38.7	0.4
	358.0	69.3	0.2
Min. angle = 25	325.9	83.4	3.9
	49.1	50.6	1.8
	91.6	82.8	1.2
	241.5	86.9	1.0
	253.1	59.6	1.0
	208.3	38.7	0.4
Min. angle = 20	325.9	83.4	3.9
	49.1	50.6	1.8
	91.6	82.8	1.2
	241.0	86.9	1.0
	253.1	59.6	1.0
	47.6	73.1	0.5
Min. angle = 15	325.9	83.4	3.9
	326.9	66.3	3.0
	49.1	50.6	1.8
	91.6	82.8	1.2
	241.5	86.9	1.0
	253.1	59.6	1.0
Min. angle = 10	325.9	83.4	3.9
	326.9	66.3	3.0
	49.1	50.6	1.8
	91.6	82.8	1.2
	241.5	86.9	1.0
	253.1	59.6	1.0

Preprints (www.preprints.org) | NOT PEER-REVIEWED | Posted: 23 April 2021 doi:10.20944/preprints202104.0641.v1

Supplementary Table S4: Automatically extracted orientations of the highway slope with different knn values

knn level	Dip direction (°)	Dip angle (°)	Density (%)
***knn* = 90**	278.9	39.6	8.0
	283.4	74.2	3.2
	319.6	84.9	0.4
	117.4	43.8	0.3
	91.8	76.2	0.2
	247.6	69.5	0.0
***knn* = 75**	276.2	39.4	8.2
	284.4	78.0	2.9
	319.3	84.7	0.4
	90.2	72.8	0.2
	118.0	38.7	0.2
	140.5	64.9	0.1
***knn* = 60**	264.5	29.3	7.6
	305.0	62.6	3.8
	286.0	87.8	1.8
	144.5	69.6	0.2
	109.4	36.2	0.2
	258.5	73.7	0.2
***knn* = 45**	257.2	30.0	9.5
	297.7	54.0	3.9
	109.6	86.1	2.0
	319.7	85.2	0.5
	145.7	64.7	0.3
	108.1	36.1	0.2
***knn* = 30**	263.5	29.4	14.3
	301.3	55.6	3.7
	108.3	85.5	2.1
	140.7	86.2	0.3
	80.4	62.0	0.2
	128.7	43.1	0.2
***knn* = 15**	261.9	29.4	21.7
	304.6	57.3	3.2
	107.9	79.0	2.0
	319.8	85.0	0.8
	148.9	61.9	0.3
	80.3	58.0	0.2

Preprints (www.preprints.org) | NOT PEER-REVIEWED | Posted: 23 April 2021 doi:10.20944/preprints202104.0641.v1

Supplementary Table S5: Automatically extracted orientations of the highway slope with different bin levels

Bin level	Dip direction (°)	Dip angle (°)	Density (%)
bin level = 12	259.9	28.8	50.0
	302.7	53.8	5.6
	100.1	86.4	4.8
	311.2	87.2	1.6
	268.4	64.7	1.6
	108.7	56.3	1.0
bin level = 10	260.2	29.0	49.3
	302.7	53.8	5.6
	100.1	86.5	4.5
	311.1	87.3	1.6
	268.4	64.6	1.5
	108.9	56.1	1.0
bin level = 8	259.7	28.7	39.5
	302.9	53.9	5.2
	100.0	86.8	3.5
	311.2	87.4	1.4
	266.7	63.2	1.1
	108.9	56.6	0.8
bin level = 6	263.5	29.4	14.3
	301.3	55.6	3.7
	108.3	85.5	2.1
	140.7	86.2	0.3
	80.4	62.0	0.2
	128.7	43.1	0.2
bin level = 4	279.5	53.5	3.2
	107.4	86.4	1.3
	204.8	70.9	0.0

Preprints (www.preprints.org) | NOT PEER-REVIEWED | Posted: 23 April 2021 doi:10.20944/preprints202104.0641.v1

Supplementary Table S6: Automatically extracted orientations of the highway slope with different minimum angles

Min. angle level	Dip direction (°)	Dip angle (°)	Density (%)
Min. angle = 35	263.5	29.4	14.3
	301.3	55.6	3.7
	108.3	85.5	2.1
	148.7	61.4	0.3
	80.4	62.0	0.2
	250.2	72.2	0.1
Min. angle = 30	263.5	29.4	14.3
	301.3	55.6	3.7
	108.3	85.5	2.1
	140.7	86.2	0.3
	80.4	62.0	0.2
	128.7	43.1	0.2
Min. angle = 25	263.5	29.4	14.3
	301.3	55.6	3.7
	108.3	85.5	2.1
	134.9	84.2	0.4
	265.2	82.7	0.3
	148.7	61.4	0.3
Min. angle = 20	263.5	29.4	14.3
	301.3	55.6	3.7
	108.3	85.5	2.1
	310.2	87.8	0.6
	92.5	69.1	0.4
	265.2	82.7	0.3
Min. angle = 15	263.5	29.4	14.3
	284.0	45.1	5.9
	301.3	55.6	3.7
	108.3	85.5	2.1
	310.2	87.8	0.6
	92.5	69.1	0.4
Min. angle = 10	263.5	29.4	14.3
	284.0	45.1	5.9
	301.3	55.6	3.7
	108.3	85.5	2.1
	98.0	79.9	1.3
	310.2	87.8	0.6

References

1. Assali, P., Grussenmeyer, P., Villemin, T., Pollet, N., & Viguier, F. (2014). Surveying and modeling of rock discontinuities by terrestrial laser scanning and photogrammetry: Semi-automatic approaches for linear outcrop inspection. Journal of Structural Geology, 66, 102-114. doi: 10.1016/j.jsg.2014.05.014
2. Besl, P. J., & McKay, N. D. (1992, April). Method for registration of 3-D shapes. In Sensor fusion IV: control paradigms and data structures (Vol. 1611, pp. 586-606). International Society for Optics and Photonics. doi: 10.1117/12.57955
3. Chen, J., Zhu, H., & Li, X. (2016). Automatic extraction of discontinuity orientation from rock mass surface 3D point cloud. Computers & Geosciences, 95, 18-31. doi: 10.1016/j.cageo.2016.06.015
4. Chen, N., Kemeny, J., Jiang, Q., & Pan, Z. (2017). Automatic extraction of blocks from 3D point clouds of fractured rock. Computers & Geosciences, 109, 149-161. doi: 10.1016/j.cageo.2017.08.013
5. Cinar, A. F., Barhli, S. M., Hollis, D., Flansbjer, M., Tomlinson, R. A., Marrow, T. J., & Mostafavi, M. (2017). An autonomous surface discontinuity detection and quantification method by digital image correlation and phase congruency. Optics and Lasers in Engineering, 96, 94-106. doi: 10.1016/j.optlaseng.2017.04.010
6. Ge, Y., Tang, H., Xia, D., Wang, L., Zhao, B., Teaway, J. W., ... & Zhou, T. (2018). Automated measurements of discontinuity geometric properties from a 3D-point cloud based on a modified region growing algorithm. Engineering Geology, 242, 44-54. doi: 10.1016/j.enggeo.2018.05.007
7. Gomes, R. K., de Oliveira, L. P., Gonzaga Jr, L., Tognoli, F. M., Veronez, M. R., & de Souza, M. K. (2016). An algorithm for automatic detection and orientation estimation of planar structures in LiDAR-scanned outcrops. Computers & Geosciences, 90, 170-178. doi: 10.1016/j.cageo.2016.02.011
8. Guo, J., Liu, S., Zhang, P., Wu, L., Zhou, W., & Yu, Y. (2017). Towards semi-automatic rock mass discontinuity orientation and set analysis from 3d point clouds. Computers & Geoences, 103(JUN.), 164-172. doi: 10.1016/j.cageo.2017.03.017
9. Hu, L., Xiao, J., & Wang, Y. (2019a). An automatic 3D registration method for rock mass point clouds based on plane detection and polygon matching. The Visual Computer, 1-13. doi: 10.1007/s00371-019-01648-z
10. Hu, S., Chen, Z., Liu, Z., Wan, C., & Huang, L. (2019b). Accuracy and reliability evaluation of 3D-LS for the discontinuity orientation identification with different registration/georeferencing modes. Marine Georesources & Geotechnology, 37(10), 1196-1204. doi: 10.1080/1064119X.2018.1542760
11. Hu, S., Huang, L., Chen, Z., Ji, Z. M., & Liu, Z. (2019c). Effect of sampling interval and anisotropy on laser scanning accuracy in rock material surface roughness measurements. Strength of Materials, 51(4), 678-687. doi: 10.1007/s11223-019-00115-3
12. Hu, L., Xiao, J., & Wang, Y. (2020a). Efficient and automatic plane detection approach for 3-D rock mass point clouds. Multimedia Tools and Applications, 79(1-2), 839-864. doi: 10.1007/s11042-019-08189-6
13. Hu, S., Liu, Z., Chen, Z., Wan, C., Tang, C., & Xiong, W. (2020b). Effect of different registration methods on precision of orientation based on RTK registration/georeferencing mode. Marine Georesources & Geotechnology, 38(4), 385-392. doi: 10.1080/1064119X.2019.1574324
14. Huang, L., Tang, H., Tan, Q., Wang, D., Wang, L., Eldin, M. A., ... & Wu, Q. (2016). A novel method for correcting scanline-observational bias of discontinuity orientation. Scientific Reports, 6(1), 22942. doi: 10.1038/srep22942
15. Huang, L., Tang, H., Wang, L., & Juang, C. H. (2019). Minimum scanline-to-fracture angle and sample size required to produce a highly accurate estimate of the 3-D fracture orientation distribution. Rock Mechanics and Rock Engineering, 52(3), 803-825. doi: 10.1007/s00603-018-1621-z
16. Huang, L., Juang, C. H., & Tang, H. (2020a). Assessing error in the 3D discontinuity-orientation distribution estimated by the Fouché method. Computers and Geotechnics, 119, 103293. doi: 10.1016/j.compgeo.2019.103293
17. Huang, L., Su, X., & Tang, H. (2020b). Optimal selection of estimator for obtaining an accurate three-dimensional rock fracture orientation distribution. Engineering Geology, 105575. doi: 10.1016/j.enggeo.2020.105575
18. Idrees, M. O., & Pradhan, B. (2018). Geostructural stability assessment of cave using rock surface discontinuity extracted from terrestrial laser scanning point cloud. Journal of Rock Mechanics and Geotechnical Engineering, 10(3), 534-544. doi: 10.1016/j.jrmge.2017.11.011
19. Kong, D., Wu, F., & Saroglou, C. (2020). Automatic identification and characterization of discontinuities in rock masses from 3D point clouds. Engineering Geology, 265, 105442. doi: 10.1016/j.enggeo.2019.105442
20. Pagano, M., Palma, B., Ruocco, A., & Parise, M. (2020). Discontinuity Characterization of Rock Masses through Terrestrial Laser Scanner and Unmanned Aerial Vehicle Techniques Aimed at Slope Stability Assessment. Applied Sciences, 10(8), 2960. doi: 10.3390/app10082960
21. Riquelme, A. J., Abellán, A., Tomás, R., & Jaboyedoff, M. (2014). A new approach for semi-automatic rock mass joints recognition from 3D point clouds. Computers & Geosciences, 68, 38-52. doi: 10.1016/j.cageo.2014.03.014
22. Riquelme, A., Tomás, R., Cano, M., Pastor, J. L., & Abellán, A. (2018). Automatic mapping of discontinuity persistence on rock masses using 3D point clouds. Rock Mechanics and Rock Engineering, 51(10), 3005-3028. doi: 10.1007/s00603-018-1519-9
23. Tang, H. M., Huang, L., Bobet, A., Ezeldin, M. A., Wang, L. Q., Wu, Y. P., & Hu, X. L. (2016). Identification and mitigation of error in the Terzaghi bias correction for inhomogeneous material discontinuities. Strength of Materials, 48(6), 825-833. doi: 10.1007/s11223-017-9829-9
24. Tang, H., Huang, L., Juang, C. H., & Zhang, J. (2017). Optimizing the Terzaghi estimator of the 3D distribution of rock fracture orientations. Rock Mechanics and Rock Engineering, 50(8), 2085-2099. doi: 10.1007/s00603-017-1254-7
25. Tang, H., Zhang, J., Huang, L., Yan, C., Hu, S., & Eldin, M. A. (2018). Correction of line-sampling bias of rock discontinuity orientations using a modified Terzaghi method. Advances in Civil Engineering, 1-9. doi: 10.1155/2018/1629039

26. Tomás, R., Abellán, A., Cano, M., Riquelme, A., Tenza-Abril, A. J., Baeza-Brotons, F., ... & Jaboyedoff, M. (2018). A multidisciplinary approach for the investigation of a rock spreading on an urban slope. Landslides, 15(2), 199-217. doi:10.1007/s10346-017-0865-0
27. Ulusay, R. (2015). The ISRM suggested methods for rock characterization, testing and monitoring: 2007–2014, Springer International Publishing, Berlin. doi: 10.1007/978-3-319-07713-0
28. Umili, G., Bonetto, S. M. R., Mosca, P., Vagnon, F., & Ferrero, A. M. (2020). In Situ Block Size Distribution Aimed at the Choice of the Design Block for Rockfall Barriers Design: A Case Study along Gardesana Road. Geosciences, 10(6), 223. doi: 10.3390/geosciences10060223
29. Wen, T., Tang, H., Huang, L., Hamza, A., & Wang, Y. (2021). An empirical relation for parameter mi in the Hoek–Brown criterion of anisotropic intact rocks with consideration of the minor principal stress and stress-to-weak-plane angle. Acta Geotechnica, 16(2), 551-567. doi: 10.1007/s11440-020-01039-y
30. Xu, W., Zhang, Y., Li, X., Wang, X., Ma, F., Zhao, J., & Zhang, Y. (2020). Extraction and statistics of discontinuity orientation and trace length from typical fractured rock mass: A case study of the Xinchang underground research laboratory site, China. Engineering Geology, 105553. doi: 10.1016/j.enggeo.2020.105553